Optimized two-layer motheye structures for MgAl$_2$O$_4$ spinel ceramic windows

CHAORAN TU,[1,*] **JONATHAN HU,**[2] **CURTIS R. MENYUK,**[1] **THOMAS F. CARRUTHERS,**[1] **L. BRANDON SHAW,**[3] **LYNDA E. BUSSE,**[3] **AND JASBINDER S. SANGHERA**[3]

[1]*Department of Computer Science and Electrical Engineering, University of Maryland Baltimore County, Baltimore, MD 21250, USA*
[2]*Department of Electrical and Computer Engineering, Baylor University, Waco, TX 76798, USA*
[3]*US Naval Research Lab, 4555 Overlook Ave SW, Washington, DC 20375, USA*
*chaoran1@umbc.edu

Abstract: We computationally study two-layer motheye nanostructures fabricated on MgAl$_2$O$_4$ spinel ceramic windows. We investigated the parameters of the structure, including height, width, and shape, in order to optimize its power transmission efficiency over a broad bandwidth. We found a two-layer motheye structure in which the cones of the upper structure have a concave shape that can theoretically achieve more than 99.8% transmission at normal incidence in the wavelength range between 0.4 μm and 5.0 μm.

1. Introduction

Motheye structures are periodic sub-wavelength structures that act as anti-reflection (AR) surfaces by gradually changing the effective refractive index at the interface between two optical media [1–3]. They were first observed in nature by Bernhard in the eyes of night-flying moths [4]. Motheye structures have been fabricated on optical surfaces using interference lithographic techniques [5–8]. Busse *et al.* [9] have reported the damage threshold of MgAl$_2$O$_4$ spinel ceramic windows with motheye AR surfaces (10 J/cm^2) can be significantly larger than the damage threshold of traditional AR-coated surfaces (4.5 J/cm^2) at 1.06 μm [9]. Motheye structures are useful in a number of applications, including increasing sunlight readability [10] (visible light), automotive glass [11] (visible light), laser systems [12] (visible to mid-infrared), fiber optics [13] (visible to mid-infrared), and photovoltaics [14,15] (ultraviolet to infrared).

One-layer motheye structures were first used 40 years ago for solar cell applications [2]. While periodic, one-layer motheye structures have proved successful in many applications [16], they are typically limited in bandwidth. In order to increase the bandwidth, it is necessary to use more complex structures [16], including random structures [9,17–19] or double-layered or double-textured structures [19–25]. We note that both strategies are commonly used in nature [16]. While the body of work on these more complex structures has grown significantly in the past five years, there has been relatively little work aimed at exploring their theoretical potential and limits. In this work, we use the finite-difference time-domain (FDTD) method [26–31] to computationally investigate the benefit of adding a second motheye layer on top of the structure that was investigated by Busse *et al.* [9] and to optimize its performance. In contrast to the one-layer structure, whose transmission spectrum only exceeds 90% over a limited range between 0.9 μm and 2.4 μm, our optimized two-layer structure achieves 99.8% transmission over the wavelength range between 0.4 μm and 5.0 μm. While similar performance can be achieved at least at normal incidence using the quarter-wavelength rule with multilayer AR coatings [32–36], this approach requires a large number of layers.

In prior work [25], we optimized the top width, the bottom width, and the height of the upper pyramids in a two-layer motheye structure. In this paper, we extend our prior work and present

a detailed study in which we find the parameters for an optimized structure with concave and convex cones on the top layer. While the full theoretical limit may not be achievable in practice with current fabrication technology, our research provides guidance for experimentalists to design and fabricate spinel ceramic windows that have high transmission over a broad bandwidth.

The rest of the paper is organized as follows: In Sec. 2, we introduce our computational model. In Sec. 3, we compute the transmission spectra for baseline structures against which to compare the improved transmission spectra of the more complex two-layer structures that are studied in the subsequent sections. In Sec. 4, we focus on simple truncated-cone structures that are placed on top of the lower layer. We calculate the transmission spectra as the cone parameters vary and find parameters that maximize the transmission spectra. In Sec. 5, we consider more complex structures, and we show that is possible to further increase the transmission by using concave cones in the upper layers. Finally, Sec. 6 contains the conclusions.

2. Computational model

In Fig. 1, we show a schematic illustration of our computational model. In our studies, we placed four cones with a circular cross section on top of the lower layer, which is a square, truncated pyramid. They are positioned so that they touch the edges of the upper square on the lower layer. The parameters of the lower layer are equal to the experimental values in [9]: $W_1 = 0.3$ μm, $W_2 = 0.6$ μm, and $H = 0.58$ μm. We used cones in the top layer, since they are more commonly used than pyramids in motheye structures [16]. Additionally, cone structures have higher transmission than pyramid structures [25]. The refractive index n that we use in our simulations is obtained from the dispersion relation for $MgAl_2O_4$ spinel [37,38] and varies between 1.723 at $\lambda = 0.5$ μm and 1.596 at $\lambda = 5.0$ μm. We considered heights h as large as 4 μm, which in this limit correspond to tall, thin structures, as shown in Fig. 1. We have not considered the mechanical or the fabrication difficulties in making these structures. Thus, our work corresponds to the theoretically possible upper limit.
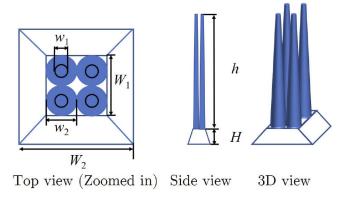

Fig. 1. Schematic view of a two layer motheye structure.

We calculate the power transmission spectra for $MgAl_2O_4$ spinel ceramic windows using the FDTD method [26–31]. We use the MEEP implementation that is freely available under the GNU General Public License [39]. In our computations, a broadband pulse is normally incident on our structures from above (air). We calculate the transmission and reflection spectra by taking a harmonic transform of the time-domain flux through surfaces lying above and below the two-layer motheye structures. We use a spatial resolution of 5 nm for all simulations, and we take advantage of the periodicity of our system to reduce the computational grid to the region that we show schematically in Fig. 2. The system that we consider is hexagonally symmetric, and

the unit cell has dimensions: $S_x = 0.8$ μm and $S_y = \sqrt{3}S_x = 1.39$ μm, in agreement with [9]. We have increased the resolution and found that the results remain the same, which indicates that our results have converged. With our current structure, we also ran additional simulations and found that transmission is polarization insensitive within the numerical error.
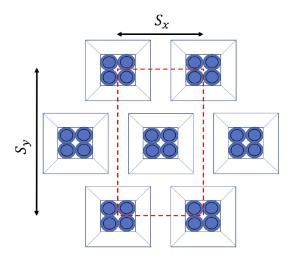

Fig. 2. Top view of a computational unit grid (red dashed line).

3. Baseline structures

In Fig. 3, we show the power transmission spectra for a one-layer motheye structure that is consistent with the experimental values in [9], but where the contribution of an untreated second surface in a transmission measurement has been removed. Some prior work shows
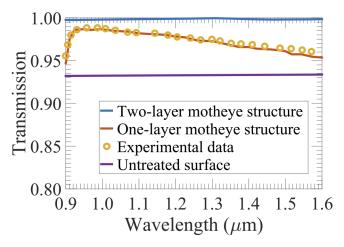

Fig. 3. The simulated power transmission spectra for a one-layer motheye structures with $W_1 = 0.30$ μm, $W_2 = 0.60$ μm, and $H = 0.58$ μm (red curve); experimental data for a one-layer motheye structures with $W_1 = 0.30$ μm, $W_2 = 0.60$ μm, and $H = 0.58$ μm (yellow circles); two-layer motheye structures with $w_1 = 0.01$ μm, $w_2 = 0.20$ μm, $h = 4.0$ μm, $W_1 = 0.40$ μm, $W_2 = 0.60$ μm, and $H = 0.39$ μm (blue curve); and untreated surface (purple curve).

the transmission through one input motheye surface [4,5,7,8], while other prior work shows transmission through both an input and output surface [6,9,11]. In this work, we consistently show the transmission through just the input motheye surface. The yellow circles and red curve in Fig. 3 show the experimental results from [9], which have been divided by 0.93 to remove the effect of an untreated output surface, and we show our simulation results for a single motheye surface with $W_1 = 0.30$ μm, $W_2 = 0.60$ μm, and $H = 0.58$ μm. We find good agreement between the simulation and experimental results. We also show simulation results for a two-layer motheye structure with $w_1 = 0.01$ μm, $w_2 = 0.20$ μm, $h = 4.0$ μm, $W_1 = 0.40$ μm, $W_2 = 0.60$ μm, and $H = 0.39$ μm. The two-layer structure has almost perfect transmission.

4.   Simple cone structure

We first consider a simple cone structure for the upper layer in which the radius of the circular cross section decreases linearly from bottom to top. We explored values of w_1 that vary from 0.01 μm to 0.20 μm, values of w_2 that vary from 0.05 μm to 0.20 μm, values of h that vary from 0.5 μm to 4.0 μm, and values of H that vary from 0.2 μm to 0.5 μm. In simulations that we show here, we kept $W_1 = 2w_2$, and we set $W_2 = 0.60$ μm, which corresponds to the experimental results in [9]. We carried out additional simulations, not shown here, in which we varied W_1, holding w_2 constant, and we found that $W_1 = 2w_2$ is optimal. We also varied W_2 by 0.1 μm, and we found that our optimized structure still yield similar results with an average transmission higher than 99.8%. The transmission spectrum is largest with the broadest bandwidth when $w_1 = 0.01$ μm, $w_2 = 0.20$ μm, $h = 4.0$ μm, and $H = 0.39$ μm. In effect, it is desirable to fill the base of the lower layer as completely as possible with cones that are as sharp as possible. We explored heights that are greater than $H = 0.39$ μm, as we show for $H = 0.5$ μm, but the results only change slightly at greater heights. It is desirable to have sharp cones and a high base, but our results also show that there are limits beyond which further increasing h and H yields little improvement.

We now examine in turn the change in transmission spectra as we allow w_1, w_2, h, and H to vary from their optimum values.

4.1.   Top width

In Fig. 4(a), we show the transmission spectra when we vary w_1. As the top width increases from $w_1 = 0.01$ μm to $w_1 = 0.20$ μm, the average transmission spectrum decreases in the entire wavelength range by more than 1.3%, and the minimum transmission spectrum decreases by more than 1.2%.

4.2.   Bottom width

In Fig. 4(b), we show the transmission spectra when we vary w_2. As the bottom width increases from $w_2 = 0.05$ μm to $w_2 = 0.20$ μm, the average transmission increases by 0.5%, and the minimum transmission increases by 0.4%.

4.3.   Height

In Fig. 4(c), we show the transmission spectra when we vary h. As the height h increases from $h = 0.5$ μm to $h = 4.0$ μm, the average transmission increases by 0.5%, and the minimum transmission increases by 0.6%.

4.4.   Base height

In Fig. 4(d), we show the transmission spectra when we vary H. As the base height H increases from $H = 0.2$ μm to $H = 0.5$ μm, the average transmission increases by 0.7%, and the minimum transmission increases by 0.5%.
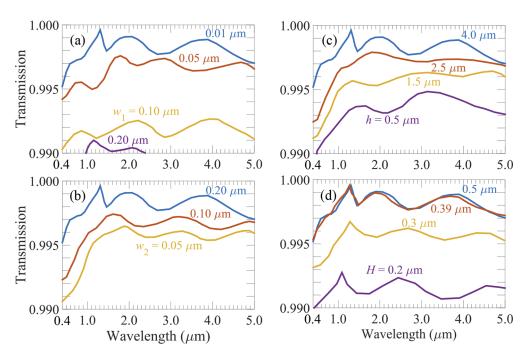
Fig. 4. Power transmission spectra with varying device dimensions: (a) $w_2 = 0.20$ μm, $h = 4.0$ μm, $H = 0.39$ μm, with w_1 varying from 0.01 to 0.20 μm; (b) $w_1 = 0.01$ μm, $h = 4.0$ μm, $H = 0.39$ μm, with w_2 varying from 0.05 to 0.20 μm; (c) $w_1 = 0.01$ μm, $w_2 = 0.20$ μm, $H = 0.39$ μm, with h varying from 0.5 to 4.0 μm; and (d) $w_1 = 0.01$ μm, $w_2 = 0.20$ μm, $h = 4.0$ μm, with H varying from 0.2 to 0.5 μm.

Based on the transmission spectra, we conclude that a two-layer spinel motheye structure with an upper layer that has a narrow top width, broad bottom width, and a large cone height will have a high transmission spectrum over a wide wavelength range. We can achieve an average transmission above 99.8% from 0.4 μm to 5.0 μm in a two-layer motheye structure that has dimensions $w_1 = 0.01$ μm, $w_2 = 0.20$ μm, $h = 4.0$ μm, and $H = 0.39$ μm. The wavelength below 400 nm is in the ultraviolet (UV) range, which requires a high resolution optical system for fabrication, and is outside the scope of this paper. To improve the transmission, we may change the shape of the cones in the upper layer, as we describe in the next section.

5. Varying the cone shape

In this section, we show results when we change the cone shape so that the radius of the cross section no longer decreases linearly from the bottom to the top. We investigated the convex and concave shapes that we show schematically in Figs. 5(a) and 5(b), respectively. The radius of the convex cones r_{convex} is given by

$$r_{\text{convex}} = \left[\frac{w_2^2}{4} - \frac{z(w_2^2 - w_1^2)}{4h} \right]^{1/2}, \tag{1}$$

and the radius of the concave cones r_{concave} is given by

$$r_{\text{concave}} = \frac{w_2}{2} - \frac{w_2 - w_1}{2} \left(\frac{z}{h} \right)^{1/2}, \tag{2}$$

where w_1 is the top width of the upper cone, w_2 is the bottom width of the upper cone, h is the height of the upper cone, and z varies from 0 to h, normal to the plane of optical incidence.

5.1. Convex cones

In Fig. 6, we show the transmission spectra of structures with convex upper cones. In Fig. 6(a), we fix w_2, h, and H equal to 0.20 μm, 4.0 μm, and 0.39 μm, respectively, and we allow w_1 to vary. The average transmission decreases by 1% and the minimum transmission decreases by 1.7% as w_1 increases from 0.01 to 0.20 μm; the larger dimension is responsible for a larger impedance mismatch for light at the interface between air and the top of the upper structure. In Fig. 6(b), we fix w_1, h, and H equal to 0.01 μm, 4.0 μm, and 0.39 μm respectively. The width w_2 increases from 0.05 μm to 0.20 μm, the average transmission coefficient increases by 0.3% and the minimum transmission increases by 0.4%. A larger w_2 results in a smaller impedance mismatch at the interface between the lower and upper structures. In Fig. 6(c), we fix w_1, w_2, and H equal to 0.01 μm, 0.20 μm, and 0.39 μm, respectively. The height h increases from 0.5 μm to 4.0 μm, the average transmission increases by about 0.5% and the minimum transmission increases by 0.7%. A larger h corresponds to a slower change of the effective refractive index along z, resulting in a smaller impedance mismatch in the upper layer motheye structure. In Fig. 6(d), we fix w_1, w_2, and h equal to 0.01 μm, 0.20 μm, and 4.0 μm, respectively. The height H increases from 0.2 μm to 0.5 μm, the average transmission increases by 0.5% and the minimum transmission increases by 0.6%.
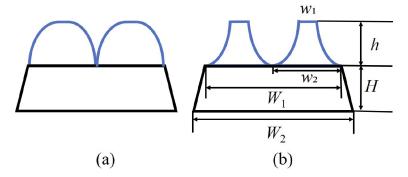

Fig. 5. Side views of different shapes: (a) convex cone; (b) concave cone.

5.2. Concave cones

In Fig. 7, we show the transmission spectra of convex cone upper structures. In Fig. 7(a), the width w_1 varies from 0.01 to 0.20 μm, while w_2, h, and H are fixed at 0.20 μm, 4.0 μm, and 0.39 μm, respectively. The average and minimum transmission decreases appreciably when w_1 is less than 0.10 μm. In Fig. 7(b), the width w_2 varies from 0.05 to 0.20 μm, while w_1, h, and H are fixed at 0.01 μm, 4.0 μm, and 0.39 μm, respectively. As is the case with straight-sided and convex cones, the average and minimum transmission increases as w_2 increases by 0.6% and 0.4%, respectively. The maximum transmission also shifts towards shorter wavelengths, and the overall transmission varies less as a function of wavelength. In Fig. 7(c), the height h varies from 0.5 to 4.0 μm with $w_1 = 0.01$ μm, $w_2 = 0.20$ μm, and $H = 0.39$ μm. The average and minimum transmission increases — in this case by 0.6% and 0.4%, respectively as h increases to its maximum value. In Fig. 7(d), the height H varies from 0.2 to 0.5 μm with $w_1 = 0.01$ μm, $w_2 = 0.20$ μm, and $h = 4.0$ μm. The average and minimum transmission increases by 0.7% and 1.0%, respectively as H increases from 0.2 μm to 0.5 μm.

The transmission for the concave cone surface shown in Fig. 7 is higher than the transmission for the convex cone structure shown in Fig. 6. In Fig. 8, we show both the average transmission and the minimum transmission over the wavelength range from 0.4 μm to 5.0 μm for the concave cone structure as a function of each quantity's magnitude. We found that the average and
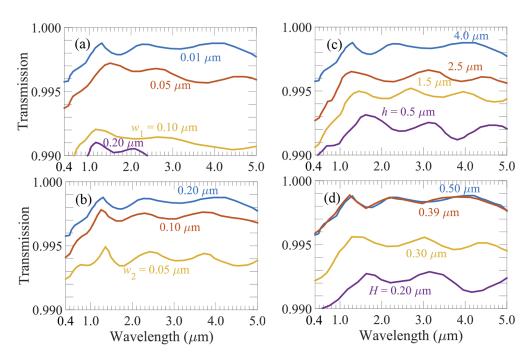
Fig. 6. Power transmission spectra for varying parameters of the convex cone two-layer motheye structures: (a) $w_2 = 0.20$ μm, $h = 4.0$ μm, $H = 0.39$ μm, with w_1 varying from 0.01 to 0.20 μm; (b) $w_1 = 0.01$ μm, $h = 4.0$ μm, $H = 0.39$ μm, with w_2 varying from 0.05 to 0.20 μm; (c) $w_1 = 0.01$ μm, $w_2 = 0.20$ μm, $H = 0.39$ μm, with h varying from 0.5 to 4.0 μm; and (d) $w_1 = 0.01$ μm, $w_2 = 0.20$ μm, $h = 4.0$ μm, with H varying from 0.2 to 0.5 μm.

minimum transmission increase as w_1 decreases, w_2 increases, h increases, W_1 decreases, or H increases.

5.3.   Comparison

We compare the two-layer concave cone motheye structure to the one-layer concave cone motheye structure. The insets in Fig. 9 show the structure shapes. The red and blue curves in Fig. 9 show the transmission of the one-layer structure and the two-layer structure, respectively. The transmission for the two-layer structure is more than 99.8% over the wavelength range between 0.4 μm and 5.0 μm. The transmission for the one-layer structure varies between 97% and 99.8% over the same wavelength range with a peak at 1.2 μm. For the blue curve using the two-layer structure, we used the optimal parameters, for which $W_1 = 0.40$ μm, $H = 0.39$ μm, $w_1 = 0.01$ μm, $w_2 = 0.20$ μm, and $h = 4.0$ μm. We fixed $W_2 = 0.60$ μm, which is consistent with current experiments. We carried out a similar optimization for a one-layer structure with the curved cones and we found that $w_1 = 0.01$ μm, $w_2 = 0.60$ μm, and $h = 4.8$ μm yields the highest transmission. The increased transmission is expected to significantly increase the damage threshold for the spinel ceramic window. The transmission results show clearly that the two-layer motheye structure has a significant advantage over the one-layer structure. While the full theoretical limit may not be achieved in practice with current fabrication technology, our research provides guidance for experimentalists to design and fabricate spinel ceramic windows that have high transmission over a broad bandwidth. Fabrication of two-layer motheye structures is challenging, but there is already experimental work that indicates that it is possible [19–25].
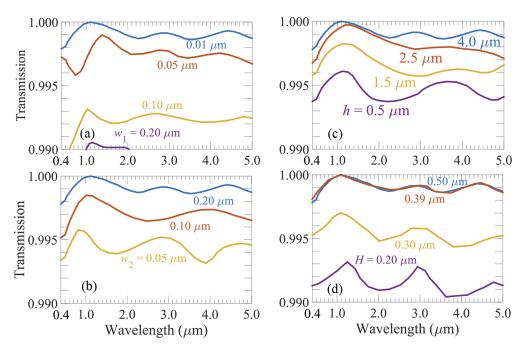
Fig. 7. Power transmission spectra for varying parameters of the concave cone two-layer motheye structures: (a) $w_2 = 0.20$ μm, $h = 4.0$ μm, $H = 0.39$ μm, with w_1 varying from 0.01 to 0.20 μm; (b) $w_1 = 0.01$ μm, $h = 4.0$ μm, $H = 0.39$ μm, with w_2 varying from 0.05 to 0.20 μm; (c) $w_1 = 0.01$ μm, $w_2 = 0.20$ μm, $H = 0.39$ μm, with h varying from 0.5 to 4.0 μm; and (d) $w_1 = 0.01$ μm, $w_2 = 0.20$ μm, $h = 4.0$ μm, with H varying from 0.2 to 0.5 μm.
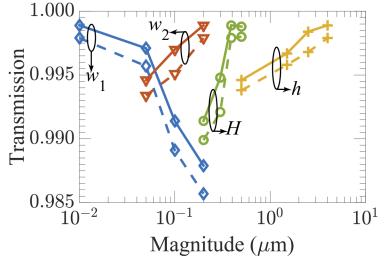

Fig. 8. The average transmission (solid lines) and minimum transmission (dashed lines) vs. each quantity's magnitude when varying w_1 (blue diamonds), w_2 (red triangles), h (yellow pluses), and H (green circles) for concave cone motheye structures under normal incidence with $W_1 = 2w_2$ and $W_2 = 0.60$ μm.
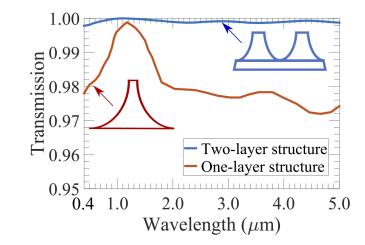
Fig. 9. Transmission versus wavelength for different optimized structures: a two-layer structure with concave cones on the top layer (blue curve) and a one-layer concave cone structure (red curve).

6. Conclusion

We used the FDTD method to computationally study the transmission of two-layer motheye structures for light that is normally incident on a spinel ceramic window. We first investigated the effect of changing the top width, bottom width and height of the upper cones, and the height of the platform in a two-layer motheye structure. We found that the transmission generally increases when the upper cones have narrow top widths, wide bottom widths and a large height, and when the platform is high. Next, we found that changing the shape of the upper cones from the regular cones into a concave cone improves the transmission spectrum. The optimal two-layer concave cone motheye structure that we found achieves a relatively uniform transmission coefficient, larger than 99.8% from 0.4 μm to 5 μm. We also found upper limits for the cone height h and the platform height H beyond which further gains are negligible.

We obtain the highest transmission for tall, thin, pointed structures on a high platform. While the optimal structures may be difficult to fabricate, our results show that there is a significant advantage in approaching these structures as closely as possible.

Disclosures. The authors declare no conflicts of interest.

Data availability. Data underlying the results presented in this paper are not publicly available at this time but may be obtained from the authors upon reasonable request.

References

1. S. Chattopadhyay, Y. F. Huang, Y. J. Jen, A. Ganguly, K. H. Chen, and L. C. Chen, "Anti-reflecting and photonic nanostructures," Mater. Sci. Eng. Rep. **69**(1-3), 1–35 (2010).
2. S. J. Wilson and M. C. Hutley, "The optical properties of 'moth eye' antireflection surfaces," Opt. Acta **29**(7), 993–1009 (1982).
3. D. Poitras and J. A. Dobrowolski, "Toward perfect antireflection coatings. 2. Theory," Appl. Opt. **43**(6), 1286–1295 (2004).
4. C. G. Bernhard and W. H. Miller, "A corneal nipple pattern in insect compound eyes," Acta Physiol. Scand. **56**(3-4), 385–386 (1962).
5. P. B. Clapham and M. C. Hutley, "Reduction of lens reflexion by the "moth eye" principle," Nature **244**(5414), 281–282 (1973).

6. J. Sanghera, C. Florea, L. Busse, L. B. Shaw, F. Miklos, and I. Aggarwal, "Reduced Fresnel losses in chalcogenide fibers by using anti-reflective surface structures on fiber end faces," Opt. Express **18**(25), 26760–26768 (2010).

7. Y. F. Huang, S. Chattopadhyay, Y. J. Jen, C. Y. Peng, T. A. Liu, Y. K. Hsu, C. L. Pan, H. C. Lo, C. H. Hsu, Y. H. Chang, C. S. Lee, K. H. Chen, and L. C. Chen, "Improved broadband and quasi-omnidirectional antireflection properties with biomimetic silicon nanostructures," Nat. Nanotechnol. **2**(12), 770–774 (2007).

8. W. Kim, G. Villalobos, C. Baker, J. Frantz, B. Shaw, S. Bayya, S. Bowman, B. Sadowski, M. Hunt, B. Rock, I. Aggarwal, and J. Sanghera, "Overview of transparent optical ceramics for high-energy lasers at NRL," Appl. Opt. **54**(31), F210–F221 (2015).

9. L. E. Busse, C. M. Florea, J. A. Frantz, L. Brandon Shaw, I. D. Aggarwal, M. K. Poutous, R. Joshi, and J. S. Sanghera, "Anti-reflective surface structures for spinel ceramics and fused silica windows, lenses and optical fibers," Opt. Mater. Express **4**(12), 2504–2515 (2014).

10. G. Tan, J. Lee, Y. Lan, M. Wei, L. Peng, I. Cheng, and S. Wu, "Broadband antireflection film with moth-eye-like structure for flexible display applications," Optica **4**(7), 678–683 (2017).

11. D. S. Hobbs, B. D. MacLeod, and J. R. Riccobono, "Update on the development of high performance anti-reflecting surface relief micro-structures," Proc. SPIE **6545**, 65450Y (2007).

12. J. Kulakofsky, W. Lewis, M. Robertson, T. Moore, and G. Krishnan, "Designing high-power components for optical telecommunications," Proc. SPIE **4679**, 198 (2002).

13. R. J. Weiblen, C. R. Menyuk, L. E. Busse, L. B. Shaw, J. S. Sanghera, and I. D. Aggarwal, "Optimized moth-eye anti-reflective structures for As_2S_3 chalcogenide optical fibers," Opt. Express **24**(10), 10172–10187 (2016).

14. S. A. Boden and D. M. Bagnall, "Optimization of moth-eye antireflection schemes for silicon solar cells," Prog. Photovoltaics **18**(3), 195–203 (2010).

15. J. Oh, H. C. Yuan, and H. M. Branz, "An 18.2%-efficient black-silicon solar cell achieved through control of carrier recombination in nanostructures," Nat. Nanotechnol. **7**(11), 743–748 (2012).

16. Z. Han, Z. Jiao, S. Niu, and L. Ren, "Ascendant bioinspired antireflective materials: Opportunities and challenges coexist," Prog. Mater. Sci. **103**, 1–68 (2019).

17. J. Choi, T. S. Lee, D. S. Jeong, W. S. Lee, W. M. Kim, K. Lee, D. Kim, and I. Kim, "Random Si nanopillars for broadband antireflection in crystalline silicon solar cells," J Phys. D: Appl. Phys. **49**(37), 375108 (2016).

18. C. Trompoukis, O. El Daif, P. P. Sharma, H. S. Radhakrishnan, M. Debucquoy, V. Depauw, K. V. Nieuwenhuysen, I. Gordon, R. Mertens, and J. Poortmans, "Passivation of photonic nanostructures for crystalline silicon solar cells," Prog. Photovoltaics **23**(6), 734–742 (2015).

19. J. W. Leem, B. Dudem, and J. S. Yu, "Biomimetic nano/micro double-textured silicon with outstanding antireflective and super-hydrophilic surfaces for high optical performance," RSC Adv. **7**(54), 33757–33763 (2017).

20. Y. Song, K. Kim, K. Choi, B. Ki, and J. Oh, "Nano/micro double texturing of antireflective subwavelength structures on inverted pyramids," Sol. Energy **135**, 291–296 (2016).

21. S. Thiyagu, B. P. Devi, and Z. Pei, "Fabrication of large area high density, ultra-low reflection silicon nanowire arrays for efficient solar cell applications," Nano Res. **4**(11), 1136–1143 (2011).

22. G. Shi, X. Zhang, J. Li, H. Zhu, Y. Li, L. Zhang, C. Ni, and L. Chi, "Fabrication of 3D biomimetic composite coating with broadband antireflection, superhydrophilicity, and double p-n heterojunctions," Nano Res. **10**(7), 2377–2385 (2017).

23. Y. Zeng, X. Chen, Z. Yi, Y. Yi, and X. Xu, "Fabrication of p-n heterostructure ZnO/Si motheye structures: antireflection, enhanced charge separation and photocatalytic properties," Appl. Surf. Sci. **441**, 40–48 (2018).

24. J. Sun, X. Wang, J. Wu, C. Jiang, J. Shen, M. A. Copper, X. Zheng, Y. Liu, Z. Yang, and D. Wu, "Biomimetic Moth-eye Nanofabrication: Enhanced Antireflection with Superior Self-cleaning Characteristic," Sci. Rep. **8**(1), 5438–5448 (2018).

25. C. Tu and C. R. Menyuk, "Anti-reflecting surfaces using two-layer motheye structures for spinel ceramic windows," in Frontiers in Optics / Laser Science, OSA Technical Digest (Optical Society of America, 2018), paper JW4A.18 (2001).

26. K. Forberich, G. Dennler, M. C. Scharber, K. Hingerl, T. Fromherz, and C. J. Brabec, "Performance improvement of organic solar cells with moth eye anti-reflection coating," Thin Solid Films **516**(20), 7167–7170 (2008).

27. J. A. Dobrowolski, D. Poitras, P. Ma, H. Vakil, and M. Acree, "Toward perfect antireflection coatings: numerical investigation," Appl. Opt. **41**(16), 3075–3083 (2002).

28. K. Yee, "Numerical solution of initial boundary value problems involving Maxwell's equations in isotropic media," IEEE Trans. Antennas Propag. **14**(3), 302–307 (1966).

29. J. Yamauchi, M. Mita, S. Aoki, and H. Nakano, "Analysis of antireflection coatings using the FD-TD method with the PML absorbing boundary condition," IEEE Photonics Technol. Lett. **8**(2), 239–241 (1996).

30. Z. Y. Yang, D. Q. Zhu, M. Zhao, and M. C. Cao, "The study of a nano-porous optical film with the finite difference time domain method," J. Opt. A: Pure Appl. Opt. **6**(6), 564–568 (2004).

31. J. D. Joannopoulos, S. G. Johnson, J. N. Winn, and R. D. Meade, *Photonic Crystals: Molding the Flow of Light* (Princeton University, 1995).

32. K. V. Popov, J. A. Dobrowolski, A. V. Tikhonravov, and B. T. Sullivan, "Broadband high-reflection multilayer coatings at oblique angles of incidence," Appl. Opt. **36**(10), 2139–2151 (1997).

33. J. D. Wheeler, B. Koopman, P. Gallardo, P. R. Maloney, S. Brugger, G. Cortes-Medellin, R. Datta, C. Darren Dowell, J. Glenn, S. Golwala, C. McKenney, J. J. McMahon, C. D. Munson, M. Niemack, S. Parshley, and G. Stacey, "Antireflection coatings for submillimeter silicon lenses," Proc. SPIE **9153**, 91532Z (2014).

34. F. Defrance, C. Jung-Kubiak, J. Sayers, J. Connors, C. deYoung, M. I. Hollister, H. Yoshida, G. Chattopadhyay, S. R. Golwala, and S. J. E. Radford, "1.6:1 bandwidth two-layer antireflection structure for silicon matched to the 190–310 GHz atmospheric window," Appl. Opt. **57**(18), 5196–5209 (2018).

35. T. Macioce, F. Defrance, C. Jung-Kubiak, S. Rahiminejad, J. Sayers, J. Connors, G. Chattopadhyay, S. R. Golwala, and S. J. E. Radford, "Multilayer Etched Antireflective Structures for Silicon Vacuum Windows," J. Low Temp. Phys. **199**(3-4), 935–942 (2020).

36. H. L. Chen, S. Y. Chuang, C. H. Lin, and Y. H. Lin, "Using colloidal lithography to fabricate and optimize sub-wavelength pyramidal and honeycomb structures in solar cells," Opt. Express **15**(22), 14793–14803 (2007).

37. W. J. Tropf and M. E. Thomas, "Magnesium aluminum spinel ($MgAlO_4$)," in *Handbook of Optical Constants of Solids II*, E. D. Palik, ed. (Academic, 1998), pp. 881–895.

38. M. Bass, C. DeCusatis, J. M. Enoch, V. Lakshminarayanan, G. Li, C. MacDonald, V. N. Mahajan, and E. V. Stryland, *Handbook of Optics, Third Edition Volume IV: Optical Properties of Materials, Nonlinear Optics, Quantum Optics* (McGraw Hill Professional, 2009).

39. A. F. Oskooi, D. Roundy, M. Ibanescu, P. Bermel, J. D. Joannopoulos, and S. G. Johnson, "MEEP: A flexible free-software package for electromagnetic simulations by the FDTD method," Comput. Phys. Commun. **181**(3), 687–702 (2010).